Gulf Stream and interior western boundary volume transport as key regions to constrain the future North Atlantic Carbon Uptake

Nadine Goris[1], Klaus Johannsen[2], and Jerry Tjiputra[1]

[1]NORCE Norwegian Research Centre and Bjerknes Centre for Climate Research, Bergen, Norway
[2]NORCE Norwegian Research Centre, Bergen, Norway

Correspondence: Nadine Goris (nadine.goris@norceresearch.no)

Abstract. As one of the major carbon sinks in the global ocean, the North Atlantic is a key player in mediating the ongoing global warming. However, projections of the North Atlantic carbon sink in a high-CO_2 future are highly uncertain due to greatly varying model results. A previous study analysed an ensemble of 11 CMIP5-models and identified two indicators of contemporary model behavior that are highly correlated with a model´s projected future carbon-uptake in the North Atlantic:

5 (i) the high latitude winter pCO_2^{sea}-anomaly, which is tightly linked to winter mixing and nutrient supply and (ii) the fraction of the anthropogenically altered carbon-inventory stored below 1000m depth, indicating the efficiency of dissolved inorganic carbon transport into and within the deep ocean. Both relationships build so-called emergent constraints, where observed contemporary indicators can be used to improve future North Atlantic carbon sink estimates.

In this study, we apply a genetic algorithm to optimize these emergent relationships by constraining the spatial extent of

10 the indicators, i.e. to identify key regions that maximise the cross-correlations between the indicators and the future carbon uptake. We pre-define the shape of the desired regions as (i) rectangles and ellipses of different sizes for the first surface-2D indicator and (ii) cuboids and ellipsoids of different volumes for the second water column-3D indicator. Independent on shape and size, the genetic algorithm persistently identifies the Gulf Stream region as optimal for the first indicator as well as the pathway of the broad interior southward volume transport for the second indicator. This is further confirmed with high

15 correlations between the North Atlantic future carbon uptake and volume transport values extracted for the central latitudes and depths of these optimal regions. Though the importance of volume transport for the carbon uptake is well known, our results go beyond traditional knowledge and identify which depth-ranges and latitudes of this volume transport are consistently of importance across the multi-model ensemble. Our study shows that regional optimisations of emergent constraint can isolate key drivers responsible for multi-model spread and furthermore provide information on where observations are most crucial

20 to constrain future projections. Moreover, a comparison of the model performance in the identified key regions and the large-scale North Atlantic indicates that models whose mean values are in good agreement with observations within one key area do not necessarily perform well when looking at another key area. This hampers the applicability of emergent constraints and highlights the need to additionally evaluate spatial model features.

1   Introduction and Motivation

25   At the heart of current investigations of the impact of possible future emissions pathways is the Coupled Model Intercomparison Project (CMIP). CMIP gathers the output of state-of-the-art climate models to a set of given experiments, designed to understand the drivers of climate change in a multi-model context. The CMIP-archive is commonly refer to in reports of the Intergovernmental Panel on Climate Change (e.g., IPCC, 2013, 2018) and has hence become fundamental for the creation of climate policies.

30   The first phase of CMIP, CMIP1, began in 1996, including 21 global coupled climate models and a handful of experiments (Meehl et al., 1997, 2000). In contrast, the sixth and latest phase of CMIP (CMIP6, Eyring et al., 2016a) includes 312 experiments (Petrie et al., 2021) and anticipated output-data from at least 100 models hosted by 40 modelling centres (Balaji et al., 2018), though not every model participated in every experiment. Moreover, the model resolution has increased substantially over the years, additional Earth system processes and components have been introduced and an increased number of variables

35   are required for each experiment (Petrie et al., 2021). Accordingly, the size of CMIP-data is increasing rapidly with a volume of 40TB related to CMIP3, 2PB for CMIP5 and an estimated 20PB for CMIP6 (Balaji et al., 2018).

Despite many progresses in climate modelling, model bias and uncertainty (i.e. spread across models) have not necessarily decreased. For example, the model-generation of CMIP6 reveals the highest range in equilibrium climate sensitivity when compared to other CMIP model-generations (Meehl et al., 2020). The combination of large data volume and partially high

40   model uncertainty in CMIP6 makes a comprehensive evaluation of associated models and simulations highly challenging. Moreover, while observational estimates inform about present and past dynamics, it is often unclear how past and contemporary model biases affect their simulated climate change signal (Eyring et al., 2019). The emergent constraint approach (e.g., Hall et al., 2019) addresses this problem by identifying a relationship between observable characteristics of the current climate (predictor) and a certain aspect of future change (predictand) that emerge within a multi-model ensemble. Based on this

45   relationship, it is possible to constrain the model ensemble, assuming that alignment with the observational estimate of the predictor is key to correctly simulate the predictand. Emergent constraints offer an attractive way of evaluating uncertain future projections. In the realm of Earth system projections, more than 50 emergent constraints have been found so far (Williamson et al., 2021). However, there are several concerns denoted when it comes to the usefulness of emergent constraints, including that a high cross-correlation between predictor and predictand can potentially reflect (i) the simplicity of a commonly used

50   model parametrization and (ii) spurious relationships (Eyring et al., 2019). Hence, a physical explanation behind the emergent constraint is key for its plausibility (Williamson et al., 2021; Hall et al., 2019).

Given a physically-plausible emergent constraint, the yielded constrained predictand is highly dependent on the observational estimate and a correct estimate of its uncertainty (Williamson et al., 2021). A highly uncertain observational constraint of the predictor will lead to a less tight estimate of the predictand. In the marine biogeochemical realm, in-situ observations

55   are often too sparse in space and time to fully capture spatial and temporal variability, including fine-scale mixing, seasonal, interannual, decadal variability, long-term trends and short-term natural variability (Wang et al., 2019). Only few platforms reach the deep ocean, though its continuous observations are necessary e.g., to confidently capture the oceanic heat and carbon

storage (Weller et al., 2019). The error occurring from the interpolation of sparse data is typically less well quantified than the observational error itself (Landschützer et al., 2020). Though the advent of biogeochemical ARGO floats gives the option to a

60 substantial contribution to the goal of a 3-dimensional image of ocean biogeochemistry (Claustre et al., 2010), this potential is still far from being fully explored. While case-studies for selected regions exists (e.g., D'Ortenzio et al., 2020), emergent constraints that focus on ocean biogeochemistry are often applied on larger ocean areas (Kessler and Tjiputra, 2016; Goris et al., 2018). Estimates of observational uncertainty are hence uncertain for emergent constraints in the realm of ocean biogeochemistry and might hamper ongoing efforts to achieve a proper constraint for climate sensitivities of ocean biogeochemical

65 variables.

It was pointed out before that emergent constraints can be used to guide observational strategies (Eyring et al., 2019). Given that there is a clear need for this in the realm of ocean biogeochemistry, we utilised two existing emergent constraints and applied a genetic algorithm to regionally optimise the area of the predictor, i. e., the observed variable. Our regional optimization explores different shapes and sizes of the sought-after area as an input and hence can be adapted for specific

70 observational campaigns such as cruises. Both emergent constraints that we regionally optimise are related to the future carbon uptake of the North Atlantic and use (i) the seasonality of the oceanic partial pressure pCO_2 and (ii) the deep ocean storage of anthropogenically altered carbon as predictors (Goris et al., 2018). Both predictors could highly gain from an improved observational strategy as data is sparse on both seasonal timescales and in the deep ocean. We therefore consider this as the optimal test case for our regional optimisation. We note, however, that our study is primarily a showcase to illustrate the

75 effectiveness of the genetic algorithm and to demonstrate the usefulness of a regionally optimised emergent constraint. Our selection of the North Atlantic basin is motivated by its critical role for the long-term anthropogenic carbon sink and as the gateway to transport carbon from surface to the deep ocean (Tjiputra et al., 2010). Further, the North Atlantic carbon uptake and dynamical features are relatively well studied such that the plausibility of our results can readily be confirmed.

This paper is organised as follows: In Section 2, we introduce the emergent constraints that we use as the base for our

80 regional optimisation as well as the genetic algorithm used for the regional optimisation and its experimental set up. When describing our results and discussing them in Section 3, we first describe the efficiency and performance of the genetic algorithm. Subsequently, we present the optimal regions for both predictors and discuss their plausibility. Finally, we present all newly found Emergent Constrains and discuss spatial differences in model performance. Our summary and conclusions can be found in Section 4.

85 ## 2 Background and experimental set-up

2.1 Emergent constraints of the North Atlantic future carbon uptake

As basis for our regional optimization, we utilise two emergent constraints that both constrain the future North Atlantic carbon uptake for an ensemble of 11 CMIP5-models under a high CO_2 future. Here, we give a short summary of these emergent constraints, for details the reader is referred to Goris et al. (2018). We note that the study of Goris et al. (2018) is concerned

90 with the "anthropogenically altered" component of the carbon cycle, defined as the outcome of the RCP8.5 experiment minus

that of the piControl experiment. All variables calculated in this manner are henceforth marked by the subscript "ant*" and can be equated to the anthropogenic component of the carbon cycle plus climate change–induced differences of the carbon cycle.

Goris et al. (2018) found that the selected model-ensemble agrees fairly well on the North Atlantic C_{ant*}-uptake of the 1990s, yet the simulated future North Atlantic C_{ant*}-uptake is highly uncertain. Here, some models simulate a future C_{ant*}-uptake of the same magnitude as that of the 1990s and other models project a future C_{ant*}-uptake that is 2-3 times higher than that of the 1990s (Fig. 1a). Goris et al. (2018) identified that discrepancies in the modelled North Atlantic future C_{ant*}-uptake arise due to differences in the efficiency of the high latitude transport of C_{ant*}-storage from the surface to the deep ocean. This transport is fuelled by deep mixed layer depths, high biological production and subsequent particle export to the deep as well as deep convection and subsequent interior ocean southward transport of C_{ant*}-storage out of the high latitudes.

Two predictors associated with the contemporary efficiency of the surface-to-depth carbon transport were identified by Goris et al. (2018). The first predictor is the mid-to-high latitude winter (November to April) pCO_2^{sea}-anomaly (Fig. 1b-c), which is tightly linked to winter mixing, nutrient supply and biological production, but also to deep convection (e.g., Olsen et al., 2008; Tjiputra et al., 2012). We note that models with a low future C_{ant*}-uptake have a negative mid-to-high latitude winter pCO_2^{sea}-anomaly. Their pCO_2^{sea} seasonal cycle is driven by temperature meaning that their C_{ant*}-uptake is strongest in winter when surface temperatures are cold. Contrarily, models with a high future C_{ant*}-uptake have a positive mid-to-high latitude winter pCO_2^{sea}-anomaly, indicating that their seasonal cycle of pCO_2^{sea} is dominated by variations of dissolved inorganic carbon (DIC) via biology and mixed layer depth. While both a DIC- and a temperature-driven pCO_2^{sea} annual cycle leads approximately to the same contemporary C_{ant*}-uptake for the considered models, a temperature-driven pCO_2^{sea} annual cycle leads to less C_{ant*}-uptake in the future. The second predictor is the fraction of the North Atlantic C_{ant*} stored below 1000m depth (Fig. 1d-e), indicating how efficient C_{ant*}-storage is transported into the deep ocean. Here, models that project a high future C_{ant*}-uptake have the majority of C_{ant*}-storage below 1000m depth, leading to a smaller fraction of C_{ant*}-storage at the surface and hence allowing for further C_{ant*}-uptake.

By comparison to the observational database, these predictors allowed to better constrain the model ensemble, and demonstrated that the models with more efficient surface-to-deep transport are best aligned with current observations (Fig. 1c,e). These models also show the largest future North Atlantic C_{ant*}-uptake, which is hence the more plausible future evolution (Fig. 1c,e). We note that, within the selected model ensemble, the cross-correlation between the contemporary mid-to-high latitude winter pCO_2^{sea}-anomaly and the future North Atlantic C_{ant*}-uptake is $r = 0.79$, while the cross-correlation between the fraction of the North Atlantic C_{ant*} stored below 1000m depth and the future North Atlantic C_{ant*}-uptake is $r = 0.94$. Though these correlations are high, the study of Goris et al. (2018) includes no regional optimization. Instead, it focuses on the broad surface areas of Mikaloff Fletcher et al. (2003) including the North Atlantic tropics (0.0°N to 17.781°N), low latitudes (17.781°N to 35.563°N), midlatitudes (35.563°N to 48.901°N), and high latitudes (48.901°N to 75.595°N) and the depth-boundary of 1000m depth as an indication for deep convection as well as for the horizon that separates between the upper and lower limbs of the Atlantic meridional overturning circulation (AMOC). Here, we apply a genetic algorithm (described in Section 2.2) to regionally optimise both predictors, i. e. to find a regionally condensed footprint of the already discovered relationship. This regional footprint might lead us even closer to the origin of the constraints but also allows to

focus on smaller and more concentrated regions, which ultimately can be utilised for observational strategies and to refine observational uncertainties. In our application of the regional optimisation to both predictors, we consider the whole North Atlantic for regional optimization of the winter pCO_2^{sea}-anomaly instead of focusing on the mid-to-high latitudes. Likewise, we consider all depth ranges of the fractional North Atlantic C_{ant*}-storage for the regional optimisation, instead of focusing on

130 the depth horizon below 1000m depth. This way, the regional optimisation can confirm or reject the previously found latitudinal boundaries and depth-ranges.

2.2 Genetic algorithm and experimental set-up

We utilize a genetic algorithm to conduct the regional optimization of the predictors. Genetic algorithms are metaheuristics inspired by the process of natural selection that can be used to design flexible optimization algorithms. The algorithm goes

135 back to Holland (1975), who created genetic algorithms drawing on the ideas from the field of biology. Since then, genetic algorithms have been developed by a growing community. The algorithms are increasingly popular due to their flexibility as they can be used in very general setting with non-differentiable or even discontinuous objective functions.

Genetic algorithms belong to the family of evolutionary algorithms and are inspired by Darwinian evolution (Sivanandam and Deepa, 2007). They mimic natural evolution through mutation, reproduction and selection to find (close-to) optimal so-

140 lutions for highly complex problems. Constitutive elements of genetic algorithms are a population formed by a number of individuals (characterized by genes and equipped with phenotypical expressions and fitness), selection of parents and reproduction (creation of offspring), mutation and selection of surviving individuals. The original population is then replaced by all or parts of the offspring. For a number of generations, the steps outlined above are repeated. In this way, the algorithm can approximate the (close-to) optimal solutions, determined by the fittest individuals. In the following paragraphs, we describe

145 the choices taken to perform the regional optimization of this study.

Before applying the genetic algorithm, we re-gridded both the winter pCO_2^{sea}-anomaly and the fractional C_{ant*}-storage values from each model on a regular 1°x1° grid. We further interpolated the fractional C_{ant*}-storage on depth-levels with a distance of 100m. That way, it is possible to construct new regions and apply them to the output of the whole model ensemble. Furthermore, we pre-select the geometrical shape of the desired region, so that it is possible to characterize regions using only

150 a few continuous genes (i.e., parameters). For both (i) the winter pCO_2^{sea}-anomaly (2D-case) and (ii) the fractional C_{ant*}-storage (3D-case), we selected two different shapes. For the 2D-case, these are rectangles aligned with the longitudinal and latitudinal axes, respectively and arbitrary ellipses. For the 3D-case, we chose rectangular cuboids aligned with the longitudinal, latitudinal and depth axes, respectively and general ellipsoids. A rectangle is encoded by four continuous genes, where the first two describe the south-western point and the second two describe the north-eastern point of the rectangle in longitude-latitude

155 coordinates (Fig. 2b). An ellipse is described by five genes (Fig. 2b), consisting of a shift vector (two genes) and a symmetric positive definite matrix (encoded by three genes). The shift vector is the center of the ellipse and the eigenvectors of the symmetric positive definite matrix are the principal axis of the ellipse. A cuboid is encoded by six genes. The first three genes describe the south-western point at the shallowest ocean depth and the second three genes describe the north-eastern point at the deepest ocean depth (Fig. 2b). Similar to the ellipse, an ellipsoid (Fig. 2b) is described by a shift vector (three

160 genes) and a symmetric positive definite matrix (six genes). The shift vector is the center of the ellipsoid and the eigenvectors of the symmetric positive definite matrix are the principal axis of the ellipsoid. Our set-up of shapes is motivated by two considerations: (i) the possibility to capture regions of interest and (ii) to have a low dimensional search space allowing for a fast optimisation. However, other options would have satisfied both criteria. Amongst them is the option to optimize a tube, so that, for example, the ship track of an upcoming cruise can be optimised.

165 For each of our applications of the genetic algorithm, we use a population of 1000 individuals evolving over 100 generations. As initialization, a population of (i) 1000 rectangles or ellipses of varying area-sizes are placed randomly across the surface of the North Atlantic ocean (2D-case) or of (ii) 1000 cuboids or ellipsoids of varying volume-sizes are placed randomly across the water columns of the North Atlantic (3D-case). Each individual gets a fitness assigned through the so-called fitness function, which is to be maximised over the course of 100 generations. For our study, the first part of the fitness function is the cross-

170 correlation of two vectors. One vector describes the future C_{ant*}-uptake of the North Atlantic (our predictand) and each entry of the vector corresponds to one member out of our ensemble of climate models. The second vector describes our predictor, which is either the contemporary winter pCO_2^{sea}-anomaly or the contemporary fractional C_{ant*}-storage within the region specified by the considered individual. The cross-correlation between first and second vector describes how tight the relationship between predictor and predictand is and higher values corresponds to a higher fitness for an individual. We additionally prescribed the

175 approximate volume or area size that the optimal region should have. Our fitness function includes a penalization to ensure compliance with the volume-condition. If a volume is not compliant with the size condition, a negative value smaller than -1, which is decreasing with the volume-violation, is added. Here, we focus on areas and volumes of i) 10-20% , ii) 20-30% and iii) 30-40% of the total size of the North Atlantic surface area or basin volume, respectively, leading in combination with rectangles, ellipses, cuboids and ellipsoids to 12 applications of the genetic algorithm. We note that the desired area can also

180 be given as total area instead of a percentage and could, for example, be the distance that the cruise can cover within a given duration. However, even when choosing a total area instead of a percentage, a range of this total area has to be given as the model resolution does not allow to reach an exact area easily. Apart from the size limitation, we are only interested in solutions where the inter-model spread in the predictor is high as we want our emergent constraint to help us to constrain model spread. Therefore, we only consider grid-point within the optimal region where the multi-model standard deviation of the predictor is

185 larger than the average multi-model standard deviation of the predictor for the whole North Atlantic.

After our initialisation, we create a new generation by applying three steps (see Fig. 2a): (1) We select a new population of 1000 individuals through a repeated tournament selection. In the tournament selection process, 10 individuals are selected at random and the fittest of these is selected (Eiben and Smith, 2003). We note that the resulting population in general contains a number of identical individuals. (2) We randomly chose 50% of the individuals of our new population (this equals a crossover

190 probability of $p = 0.5$) as parents, create two offspring for each pair of parents and use the offspring to replace their parents. This leads to a population of 500 selected individuals and 500 offspring. To create an offspring, we use a one point crossover with random position (see Fig. 2c), i. e. within the sequence of genes of both parents, a crossover site is selected at random. If, for example, an individual is defined by 4 genes and the crossover site is between the first and the second gene, then the first gene of one offspring will be defined by one parent, while the second to fourth gene is defined by the other parent (Sastry

195 et al., 2005). (3) We mutate 20% of the revised population (this equals a mutation probability of $p = 0.2$) and replace the corresponding individuals with their mutations. We realise mutation using Gaussian mutation, where a vector of Gaussian noise is added to the vector of genes (Kramer, 2017). As Gaussian noise we choose a mean of zero and a standard deviation of 0.05. After these three steps, we have a new generation consistent of selected copies, selected and mutated copies, offspring and mutated offspring. Subsequently, the fitness of each individual of our new generation is evaluated. The assigned fitness

200 is then utilised for creation of another new generation. This algorithmic sequence is illustrated in Fig. 2a. For the purpose of our study, we set the number of iterations to be fixed to 100 and stop the algorithm afterwards. The fittest individual of all generations is then defined to be our (close-to) optimal solution.

3 Results and discussion

3.1 Towards an optimal solution in 100 iterations

205 Cross-correlations between the simulated values of the future North Atlantic C_{ant*}-uptake and values of both predictors within the optimal regions identified by the genetic algorithm are significantly improved as compared to the original emergent constraints (see Fig. 3). In the 2D-case, the original cross-correlation of $r = 0.79$ is improved to $r = 0.863$, $r = 0.855$ and $r = 0.848$ for the rectangle solutions with 10-20%, 20-30% and 30-40% of North Atlantic surface area, respectively and $r = 0.863$, $r = 0.856$ and $r = 0.852$ for the ellipse solutions with corresponding area sizes. For the 3D-case, the already high original

210 cross-correlation of $r = 0.94$ is still improved to $r = 0.972$, $r = 0.966$ and $r = 0.966$ for the cuboid solutions with 10-20%, 20-30% and 30-40% of North Atlantic volume size, respectively, and $r = 0.987$, $r = 0.975$ and $r = 0.968$ for the ellipsoid solutions with corresponding volume sizes. We note that, in general, higher cross-correlations are achieved for smaller areas or volumes due to more placement possibilities. While this is not surprising, this might lead to the desire to use shapes that are even smaller than our predefined volumes and area-sizes. For our application, however, we advice against using shapes of very limited vol-

215 ume. This is based on the fact that we are searching for areas that provide a fingerprint of the original emergent constraints for the North Atlantic future C_{ant*}-uptake, which are based on features that are associated with the large scale ocean circulation. While the algorithm would be able to find high cross-correlations for shapes of smaller size, it would be difficult to assign the desired outcome to those large-scale circulation features and to assign a dynamical interpretation to the so-obtained optimal regions.

220 For the rectangle solutions, the first iteration of the genetic algorithm reaches already cross-correlation of $r = 0.862$, $r = 0.853$ and $r = 0.847$ for area-sizes of 10-20%, 20-30% and 30-40%, respectively and only offers improvements in the fourth decimal point afterwards (Fig. 3a). After four iterations, there is subsequently no improvement in the first 10 decimal points. For the ellipse solutions, the first iteration yields cross-correlations of $r = 0.855$, $r = 0.849$ and $r = 0.850$ for area-sizes of 10-20%, 20-30% and 30-40% and only improvements in the third decimal point are subsequently achieved. In contrast to the rectangle

225 solutions, the genetic algorithm converges slower for the ellipse solutions and, for the area-size of 30-40%, no subsequent improvement in the first 10 decimal points is only reached after the 90th iteration. In general, for the 2D-case, the fast speed of

convergence can be traced back to the limited area that the genetic algorithm operates in and the associated limited options for placement.

The first iteration of the cuboid-application of the genetic algorithm reaches already cross-correlations of $r = 0.960$, $r = 0.959$

230 and $r = 0.964$ for 10-20%, 20-30% and 30-40% of North Atlantic volume size (Fig. 3b). Subsequently, only improvements in the third decimal place are achieved and after 10 iterations there is no improvement in the first decimal points. Compared to the convergence of the rectangle solutions, the convergence of the cuboid-solutions is a bit slower due to more placement options throughout the water column.

In contrast to the cuboid solutions and all applications of the 2D-case, the smaller ellipsoid solutions show a slightly different

235 convergence-behaviour. Here, the cross-correlations are still significantly increasing at the end of our application of the genetic algorithm. At the same time, the maximum cross-correlation of the smaller ellipsoids during our execution of 100 iterations are 0.015 and 0.009 higher than those of the smaller cuboids. We assign both the slow speed of convergence as well as the improved cross-correlations of the smaller ellipsoid to the higher degrees of freedom as well as to more placement options as the smaller-volume ellipsoids have the option to be tilted within the water column.

240 ## 3.2 Optimal regions for the winter pCO$_2^{sea}$-anomaly and their physical explanation

The optimal regions found by the genetic algorithm for the winter pCO$_2^{sea}$-anomaly (2D-case) all have their southern boundary at 28°N or 29°N, independent on predefined shape and size (Fig. 4). Their northern boundaries vary between 43°N and 53°N, with larger optimal areas reaching further north. Longitude-wise, all optimal areas are placed in the western part of the North Atlantic. Here, their western and eastern boundaries vary dependent on the predefined size and shape of the optimal area. Yet,

245 the area between 73°W and 30°W and between 29°N and 42°N is enclosed by all optimal areas and is hence central for the considered emergent constraint. This central area is very similar to the optimal rectangle and ellipse covering 10-20% of the North Atlantic area size, which yield the highest cross-correlations when compared to the optimal rectangles and ellipses with larger surfaces, respectively (see Section 3.1). We note that for the optimal areas and their given size-requirements a placement further south was not possible as only grid-points where the multi-model standard deviation of the predictor is larger than that

250 the mean multi-model standard deviation of the predictor of the North Atlantic are eligible for our optimal regions (see Section 2.2). Non-eligible points are illustrated with different shades of blue in Fig. 4b-d. It can be readily seen that our requirements for eligible grid points excludes the lower latitudes of the North Atlantic from being chosen for placement of the optimal region. However, our eligibility criterion indicates that, for the lower latitudes, the multi-model ensemble agrees relatively well on the seasonal forcing of the winter pCO$_2^{sea}$-anomaly, so that it is not necessary to constrain the model ensemble here.

255 As noted in the introduction, a physical explanation behind the emergent constraint is of high importance for its plausibility (Williamson et al., 2021; Hall et al., 2019). Our predictor, the winter pCO$_2^{sea}$-anomaly, is a measure of seasonal features of pCO$_2^{sea}$, which are tightly related to our predictand (the future C_{ant*}-uptake), as the seasonal cycle of pCO$_2^{sea}$ indicates through which processes C_{ant*}-uptake occurs in a given model (see Section 2.1 and Goris et al., 2018). Our identified optimal regions for the predictor have the aim to point out key regions, where the simulated differences in the winter pCO$_2^{sea}$-anomaly are

260 especially well related to a model's future North Atlantic C_{ant*}-uptake. Based on multi-model mean and standard deviation

of the contemporary winter pCO_2^{sea}-anomaly (Fig. 4), it is apparent that the model spread is increasing when going further north and that the disagreement in the seasonal drivers of pCO_2^{sea} only appears in the mid-to-high latitude North Atlantic. We note that the difference in contemporary seasonal cooling/warming between models is not as prominent as their contemporary difference in mixed layer depth and biological activity (Goris et al., 2018). We expect large scale circulation features to be

265   an important driver of these model differences as these are directly related to nutrient supply and deep mixing. Based on this logic, the identified optimal regions seem reasonable as they all cover a major part of the Gulf Stream. The Gulf Stream is a key part of the warm and upper branch of the Atlantic Meridional Overturning Circulation (AMOC), which transports waters from the low-latitude North Atlantic via the Gulf Stream, the North Atlantic Current (NAC) and the Irminger Current to the high latitude North Atlantic, thereby releasing heat to the atmosphere (e.g. Rhein et al., 2011). Along this path, deep mixed

270   layers are formed via wind-driven velocity shears but also via heat-loss to the atmosphere, which becomes more prominent in higher latitudes where it leads to deep convection (e.g. Rhein et al., 2011). The strength of the Gulf Stream and its extension is not only an important driver of the amount of heat that is transported from low to high latitudes and the strength of deep convection in high latitudes but also for transporting high-nutrient thermocline waters from low to high latitudes (the so-called nutrient-stream, see e.g. Williams et al., 2011) and hence for the strength of the winter pCO_2^{sea}-anomaly. In line with this, the

275   highest multi-model standard deviation of the contemporary winter pCO_2^{sea}-anomaly follows the path of the NAC, which is the immediate Gulf Stream extension. In first instance, it seems surprising that not all optimal regions cover the path of this high standard-deviation, but that the smallest optimal regions are placed directly at the southwestern boundary of it, which coincides with the beginning of the Gulf Stream. However, we note that high multi-model standard deviations might also indicate a slightly different placement of currents between models and that the paths of Gulf Stream and NAC in the open

280   ocean are influenced by decadal variations, which might not be in phase within the model ensemble. The optimal regions cover those latitudes before and where the Gulf Stream starts to separate from the coast and where the spatial path of the current is therefore less variable within models. Additionally, we note that such a placement seems reasonable as biological production becomes more dominant further north. Here, different ecosystem model-parametrisations get a larger imprint on the simulated contemporary winter pCO_2^{sea}-anomaly, such that the cross-correlations between predictor and predictand are not only based

285   on surface temperature, available nutrients and mixed layer depth.

We use further calculations to support the argument that these optimal regions capture the influence of the upper branch of the AMOC, specifically the Gulf Stream, on the simulated contemporary winter pCO_2^{sea}-anomaly and hence on our predictand, the future North Atlantic C_{ant*}-uptake. For this, we calculate the cross-correlation between our predictand and the strength of the upper AMOC branch (see appendix B) at 30°N, as this is a central latitude in our identified optimal regions. As we consider

290   this volume transport only in terms of driving the contemporary winter pCO_2^{sea}-anomaly, we expect the transport within the mixed layer depth to be key. Indeed, when calculating cross-correlations between 10-year running averages of the accumulated northward volume transport between surface and different depths at 30°N and our predictand, we identify cross-correlations to be highest for the accumulated northward volume transport between surface and 500m. The cross-correlations get worse for both shallower and deeper depths when varying the lower boundary of the northward volume transport in depth-intervals

295   of 100m (Fig. 5a). We note that cross-correlations between 10-year running averages of our predictand and the northward

volume transport between surface and 500m stay between $r = 0.845$ and $r = 0.921$ for all considered time-periods (Fig. 5), with a cross-correlation of $r = 0.883$ for the 1990s. This value is slightly above the cross-correlations between the modelled contemporary winter pCO_2^{sea}-anomaly in our optimal regions and the predictand.

In order to quantify that these high cross-correlations between our predictor and the accumulated northward volume transport
300 between surface and 500m are a specific feature of our identified optimal regions, i.e. the Gulf Stream region, we further vary the latitude of the northward volume transport in our calculations in latitude-intervals of 5° (Fig. 5b). We find that cross-correlations are highest when utilising 10-year running averages of the northward volume transport between surface and 500m at 25°N and 30°N with cross-correlations getting worse for latitudes further north and south. Specifically between 30°N and 35°N, the cross-correlations are decreasing rapidly. For most of the considered decades, cross-correlations are slightly higher
305 at 25°N than at 30°N. However, this latitudinal band contains no eligible grid-points in the Gulf Stream region, so that the genetic algorithm could not identify it to be part of an optimal region. We conclude that it is indeed in the Gulf Stream region where cross-correlations between our predictor and the predictand are exceptionally high. We hence deem the identified optimal regions for the contemporary winter pCO_2^{sea}-anomaly to be plausible and find these regions to be characteristic of the northward volume transport of a model, governing its surface temperature distribution, available nutrients and mixed layer depths not only
310 at the specified latitudes of the optimal regions, but along the path of the Gulf Stream, NAC and Irminger currents from low-to-high latitudes. We would like to additionally denote that cross-correlations between our predictand and 10-year running averages of the maximum northward volume transport at our central latitude of 30°N stay between $r = 0.652$ and $r = 0.870$ for all considered time-periods. A commonly used metric in modelling studies, i. e., the maximum northward volume transport at 40°N yields cross-correlations with the future North Atlantic C_{ant*}-uptake between $r = 0.575$ and $r = 0.790$ for all considered
315 time-periods. Hence, when inferring from maximum AMOC-strengths to the North Atlantic carbon sink, the relationship might not be as strong as commonly assumed. We hence propose to instead focus on the northward volume transport within the mixed layer at latitudes between 25°N and 30°N.

3.3 Optimal regions for the fractional C_{ant*}-storage and their physical explanation

In the case of cuboids-solutions, all optimal areas identified by the genetic algorithm for the contemporary fractional North
320 Atlantic C_{ant*}-storage (3D-case) are placed in the western part of the North Atlantic (Fig. 6c) with a common western boundary at 96°W and southern boundaries at 19°N (smallest cuboid) or 18°N (larger cuboids). Their northern and eastern boundaries vary between 34°N-50°N and 61°W-31°W, respectively, with larger cuboids reaching both further north and east. With the given size-requirements and the fact that only grid-points where the multi-model standard deviation of the predictor is larger than the mean standard deviation of the North Atlantic are eligible for our optimal regions (see Section 2.2), a placement of the
325 optimal cuboids further south is unlikely. We note that the eligibility of grid-points is considered per depth-layer, such that the illustrated depth-integrated values of the multi-model standard deviation (Fig. 6b) only give a first indication of eligible points. The genetic algorithm identified the optimal depth-ranges for the cuboids to be 700-4700m for the smallest cuboid as well as 800-4900m for the larger cuboids. Hence, the optimal cuboids of larger volumes are enclosing the optimal cuboids of smaller volumes, such that the smallest cuboid is enclosed by all cuboids. As the cross-correlations between the simulated future North

330   Atlantic C_{ant*}-uptake and the fractional C_{ant*}-storage within the optimal cuboids is also highest for the smallest cuboid (see
Section 3.1), we consider its enclosed volume to be central for our emergent constraint.

For the ellipsoids, the optimal depth-ranges identified by the genetic algorithm are 0-4700m for the smallest, 0-5000m for
the medium-sized and 500-5000m for the largest ellipsoid. The surface positions of the vertical principal axis of the smallest
and the medium-sized ellipsoids are in the eastern North Atlantic around 25°W/40°N and they tilt in south-west direction with

335   depth until being positioned in the western North Atlantic at around 75°W/25°N for their deepest points (Fig. 6d-e). While the
vertical principal axes of the largest ellipsoid also tilts in direction south-west with depth, its position is already in the western
North Atlantic for its shallowest point (Fig. 6f).

Our predictor, the contemporary fractional North Atlantic C_{ant*}-storage is a measure for the efficiency of carbon sequestra-
tion (see Goris et al., 2018), which reflects not only the strength of high latitude deep convection and sinking organic particles,

340   but also of southward volume transport of C_{ant*} in deeper ocean depths. This feature is tightly related to our predictand, the
future North Atlantic C_{ant*}-uptake, as these pathways of carbon sequestration ultimately determine how much C_{ant*}-storage
is efficiently removed from the high latitude North Atlantic ocean surface and hence how much C_{ant*} can subsequently be
taken up across the air-sea interface. Here, a more efficient carbon sequestration, i. e. less storage of C_{ant*} in shallower depths
and more storage in the deeper ocean leads to the potential for more C_{ant*} uptake in a high CO_2 future.

345   As the ellipsoids can be tilted within the water volume, the associated optimal regions have the option to follow water masses
more closely. Their optimal solutions allow us to visually quantify if the reasoning of the predictor being a measure of pathways
of carbon sequestration (see Goris et al., 2018) holds. While the placements of the optimal ellipsoids in shallower ocean layers
are still influenced by mixed layer dynamics and the pathways of carbon sequestration are difficult to identify, the optimal
ellipsoids are placed in central areas of the simulated fractional C_{ant*}-storage pathways for deeper layers. We note that the

350   spatial gradients of the fractional C_{ant*}-storage multi-model mean (displayed for different depth in supplementary Figs. S01
and S02) are consistent with the theory that the deeper and southward branch of the North Atlantic volume transport can be
divided into (i) a fast and narrow boundary pathway and (ii) a relatively slow and broad interior pathway west of the North
Atlantic ridge (Gary et al., 2011, and references therein). However, the multi-model standard deviation of the fractional C_{ant*}-
storage as displayed in Fig. 6b (and additionally displayed for different depths in supplementary Figs. S03 and S04) indicates

355   that the models do not agree on the strength of this southward transport, neither for its slow nor for its fast component. For
ocean depths below 1000m, the optimal ellipsoids consistently point towards the areas of the relatively slow and broad interior
pathway west of the North Atlantic ridge with both high fractional C_{ant*}-storage multi-model mean values and standard
deviations. We hence deem the optimal ellipsoids to be in accordance with the previous reasoning of Goris et al. (2018).

The cuboid-solutions are implemented in a way that prevents them from being tilted within the water volume and they hence

360   can not follow the C_{ant*} sequestration pathway as closely as the ellipsoid solutions. We note, however, that all optimal cuboids
seem to point roughly towards the southernmost points that the relatively slow and broad interior southward transport of C_{ant*}
reaches to, though the narrow and fast southward transport of C_{ant*} reaches further south (both are indicated through the
horizontal gradient in the fractional C_{ant*}-storage multi-model mean as illustrated in Fig. 6b and supplementary Figs. S01 and

S02). This placement seems to support our argument that the optimal cuboids-solutions capture the influence of the transport
365   pathways of the carbon sequestration.

As previously done in the 2D-case, we use further calculations to support our argument with respect to the optimal cuboids. In
detail, we calculate cross-correlations between our predictand and the streamfunction volume transport at 26°N (see appendix
B), as this is the latitudinal mid-point of the smallest cuboid and hence a central latitude in our identified optimal cuboids. To
validate the depth-boundaries identified by the smallest and central cuboid, we set one boundary of the volume transport to be
370   one of the identified depth-boundaries of the cuboid, while we vary the other depth-boundary (Fig. 7a-b). Cross-correlations
between 10-year running averages of the accumulated volume transport in different depth-ranges at 26°N and our predictand
show that cross-correlations are highest for the accumulated southward volume transport between 900-4700m when varying the
upper depth boundary (Fig. 7a) and between 700-5300m (or even deeper) when varying the lower depth boundary (Fig. 7b).
While this seems to indicate that the depth-boundaries of the cuboids are not optimal, we note that the cross-correlations
375   obtained for upper depth boundaries of 900m and 700m are relatively similar and a strong decline in cross-correlations only
appears for an upper depth boundary above 500m. Moreover, the C_{ant*} southward transport is strongly influenced by the
amount of C_{ant*} that is available for transport in a specific depth-layer and while the lower depth boundary of 5300m reaches
higher cross-correlations between 10-year running averages of the southward volume transport and the predictand, the amount
of C_{ant*} that can be transported in these deep depth layers is negligible. Additionally, there are no eligible grid-points in these
380   very deep layers.

When considering the streamfunction volume transport within the depth-boundaries given by the smallest optimal cuboid
and varying its latitudes (Fig. 7c), we find that the 10-year running averages of volume transport at the identified mid-latitude
of the smallest cuboid offers significantly higher cross-correlations with our predictand than the volume transport further north.
This points towards the optimal cuboids capturing an important latitude of the southward interior C_{ant*}-transport. However,
385   the volume transport south of the cuboid's placements offers slightly higher cross-correlations with the predictand. Yet, in
these latitudes south of our cuboids, the amount of deep C_{ant*}-storage available for southward transport is small and there are
moreover very few eligible grid-points in these latitudes. Under the conditions given to the genetic algorithm, the identified
depth ranges and latitudes hence seem plausible. Cross-correlations between our predictand and 10-year running averages of
the southward volume transport at the identified depth-ranges and latitudinal mid-point of the smallest cuboid are between
390   $r = 0.690$ and $r = 0.859$ for all time-periods and $r = 0.771$ for the analysed time-period 1997-2007. While the identified cross-
correlations indicate a strong link between southward volume transport and our predictand, we note that our original predictor,
the fractional C_{ant*}-storage offers an better relationship with our predictand. This comes as no surprise as the depth-distribution
of the C_{ant*}-storage plays a big role in its southward transport.

3.4   Newly identified emerging relationships and their implications

395   Based on the high cross-correlations between our indicators in the identified optimal areas and the future North Atlantic C_{ant*}
uptake and due to the dynamical plausibility of these relationships, we identify the values of our indicators in the optimal areas
as new and additional predictors. Furthermore, we found the upper (0-500m) North Atlantic northward volume transport at

30°N (2D-case) and the deep (700-4700m) North Atlantic southward volume transport at 26°N (3D-case) to be powerful and plausible predictors. Now, we use observational estimates of our new predictors to constrain our predictand. This procedure is

400 based on the assumption that a correct simulation of our new predictors is fundamental for being able to correctly simulate the future North Atlantic C_{ant*} uptake and can be used as a necessary condition for its estimation. For details of the method that we utilise to calculate the unconstrained and observationally constrained estimates of the future North Atlantic C_{ant*} uptake, the reader is referred to Bourgeois et al. (2022). We note that, for the volume transport, the spatially closest observations available are those from the RAPID array (see Appendix A) at 26.5°N, starting from April 2004. In order to be able to use these

405 observations as a constraint, we consider both volume transport related predictors at 26°N and for the time period 2005-2014. Both our dynamical explanation of the emergent relationship and the associated high cross-correlations are not fundamentally changed by this (Fig. 5).

The unconstrained estimate of our model ensemble yields a mean value of 0.5±0.25 PgC/yr for the future North Atlantic C_{ant*} uptake. When applying our regionally optimised predictors, the observational constraints correct the unconstrained

410 mean values towards higher mean values between 0.57 PgC/yr and 0.79 PgC/yr (see Table 1). We note that all newly obtained constrained values for the future North Atlantic C_{ant*} uptake are consistent which each other, i.e. the uncertainties around the constrained mean values are large enough for the solutions to not contradict each other. In line with this, there is one model that satisfies the observational constraint of all our predictors, that is CESM1-BGC (Fig. 8). Nevertheless, it can readily be seen that our observational constraints for the upper ocean predictors are systematically identifying models with a higher future

415 North Atlantic C_{ant*} uptake to be dynamically 'correct' than those for the deep ocean predictors. This is also reflected in our constrained mean values, which are 0.09-0.22PgC/yr higher for the upper ocean predictors ((see Table 1). Moreover, we note that the upper ocean predictors positioned further south have models with lower future North Atlantic C_{ant*} uptake closest to their mean observational value than those positioned further north. The observational mean value of the winter pCO_2^{sea}-anomaly increases by 5.85μatm (7.18μatm) between the smaller and the largest rectangles (ellipses). However, the average

420 value of the winter pCO_2^{sea}-anomaly of the four models that are closest to the observational mean values only increased by 1.89μatm (3.99μatm). This indicates that the south-north gradient of the modelled winter pCO_2^{sea}-anomaly is not steep enough, i.e. that the modelled northwards-propagation of related properties is too weak. However, the uncertainties around the observational estimates of the winter pCO_2^{sea}-anomaly are large and do not allow us to be certain about this south-north gradient in the upper ocean model performance. We note that, in this study, the uncertainties around the observational estimates of the

425 winter pCO_2^{sea}-anomaly have been estimated very roughly and generously. Assuming that we had utilised our identified optimal areas to gain new and narrower observational uncertainties, then our new observational constraints could be utilised to identify a comparatively weak northward propagation of the winter pCO_2^{sea}-anomaly within our model ensemble. Interestingly, some of the deep ocean predictors are also placed slightly further south than the upper ocean predictors, which can partly explain that they identify models with lower future North Atlantic C_{ant*} uptake to be correct (when compared to the upper ocean

430 predictors). The difference between the upper ocean predictors and the deep ocean predictors reduces from 0.09-0.22PgC/yr to 0.09-0.16PgC/yr when only considering the southern upper ocean predictors (smallest ellipse/rectangle and upper ocean northwards transport at 26°N).

Emergent constraints of larger regions like the North Atlantic might deem a model to be the fittest due to its ability to simulate values within the observational uncertainties. Yet, we show that this model's gradient of the observed quantity within
435 the considered region might be a misfit. This is of high importance for dynamical predictors that capture, for example, a transport from north to south. Here, the north-south distribution of the predictor is in fact an expression of its dynamical correctness. It is moreover especially important for predictands that are not evenly distributed within the considered region. For example, the future C_{ant*} uptake is not uniformly distributed over the North Atlantic but there is substantially higher C_{ant*} uptake in higher latitudes such that a misfit in the north-south gradient of the winter pCO_2^{sea}-anomaly will have consequences
440 for the correctness of the constrained value. Whenever spatial distributions are important for the dynamic of the emergent constraint, we propose therefore to always additionally evaluate the spatial gradient of the bias of the predictor within the considered area. We note that the temporal robustness of an emergent constraint is also of importance, but this information is frequently analysed in studies concerned with emergent constraints (see Bourgeois et al., 2022).

4 Summary and conclusions

445 We applied a genetic algorithm to regionally constrain the predictors of two emergent constraints in the realm of the ocean carbon cycle, with the objective to enhance our understanding of key processes driving the uncertainties in the projected future anthropogenically altered carbon (C_{ant*}) uptake in the North Atlantic. The predictors of these emergent constraints are (i) the contemporary winter pCO_2^{sea}-anomaly, which is a surface quantity (2D-case) and (ii) the fraction of the North Atlantic C_{ant*}-storage, which is a surface-to-interior ocean quantity (3D-case). Both predictors relate to a model's ability to efficiently
450 remove C_{ant*} from the ocean's surface into the deep ocean.

The genetic algorithm was primarily adopted to find optimal regions for both predictors, such that cross-correlations between the regionally-optimized predictor-values and predictand-values are maximised. As emergent constraints are utilised to constrain the model spread, we only allowed the genetic algorithm to consider grid-points where the multi-model standard deviation of the simulated predictors was larger than average. For the regional optimisation, we pre-defined a suite of different
455 shapes and sizes, such that the genetic algorithm had to identify optimal ellipses and rectangles for the 2D-case and optimal ellipsoids and cuboids for the 3D-case with different size and volumes, respectively.

Our results indicate that the genetic algorithm converges quickly. After 100 iterations, the optimal solutions of the genetic algorithm provided higher cross-correlations than the original emergent constraints. With multi-model cross-correlations between 0.848 and 0.863, the regional solutions of the 2D-case were at least 0.058 higher than those of the original emergent
460 constraint. The regional solutions of the 3D-case had cross-correlations between 0.966 and 0.987 and offered an improvement of 0.026-0.047 in comparison to those of the original emergent constraint. The optimal predictor regions pointed towards the Gulf Stream area at around 30°N to be central for our emergent constraint (2D-case) as well as the interior ocean pathway of the southward volume transport (3D-case). Both identified areas are plausible. The Gulf Stream is fundamental in transporting heat and nutrients to the north and is therefore key in determining a model's mixed layer depth as well as its productivity in high
465 latitudes and hence its C_{ant*}-uptake. The interior ocean southward volume transport is fundamental for transporting C_{ant*}-

saturated surface watermasses to the deep ocean and hence allowing for further high latitude C_{ant*}-uptake. These dynamical justifications led to the detection of two additional qualified predictors of the future North Atlantic C_{ant*} uptake: the upper ocean northward volume transport between surface and 500m depth at 30°N and the deep ocean southward volume transport between 700m and 4700m at 26°N. We note that the commonly used depth range of the northward maximum volume transport

470 (surface to depth of maximum) did not allow for such high cross-correlations, neither at 26°N nor at 40°N. This indicates that the relation of maximum northward volume transport to the ocean carbon sink is not as robust as often assumed.

To our knowledge, this is the first time that a regional optimisation of emergent constraints has been carried out. The results are of high value as the use of emergent constraints in the realm of climate projections has gained a lot of momentum in the last decade (see Williamson et al., 2021, for a review of existing emergent constraints for climate sensitivites) due to the fast

475 growing number of models taking part in coordinated model exercises associated with future projections (e.g. Balaji et al., 2018). Though invaluable progress has been made through automated observational platforms like Argo (Argo, 2000) and analysis tools like ESMvaltool (Eyring et al., 2016b), observational networks and analyses of these future projections are not growing in the same speed. Here, our regional optimisation of existing emergent constraints can be used to guide future monitoring strategies. We show this for the North Atlantic, where our results point towards the already employed RAPID array and

480 prove that the algorithm is able to provide meaningful results. We note, however, that the RAPID array takes purely physical observations, though our localised emergent constraints show that additional measures of carbon-storage would fundamentally improve our understanding of the C_{ant*}-uptake in the North Atlantic. For other ocean basins, we foresee that a similar application of our regional optimisation on existing emergent constraints could be of fundamental value for the employment of further observational instruments.

485 Our regional optimisation of two existing emergent constraints of the future North Atlantic C_{ant*} uptake allowed moreover for a better understanding of modelled dynamics of the predictors. Though a typical emergent constraint should already have a solid physical background, its predictor is usually averaged aver a large area such that the optimal areas found by the algorithm help to refine this knowledge. Our regional optimisation and the newly identified emergent constraints pointed us towards the fact that dynamical features are often inherently coupled to spatial distributions. Hence, model performance of this

490 dynamic can not be captured by one single averaged value as usually done for emergent constraints. In our case, the regional optimisation confirmed that a correct simulation of the upper ocean and interior ocean volume transport is fundamental for a correct estimate of the future North Atlantic C_{ant*} uptake. However, our results indicate that models that perform well for the upper ocean volume transport might not perform well for the interior ocean volume transport and that models do not capture the south-north gradient of the upper ocean northward volume transport well. It is questionable if a model that simulates the

495 average upper ocean northward volume transport within observational constraints but not the related dynamical features like the south-north gradient of that transport can be considered a well-performing model. In future studies, we henceforth advise to combine the average values of the emergent constraint with a measure of spatial performance relating to the dynamical feature in question.

Code and data availability. The code of the genetic algorithm introduced and utilised in this paper can be found in the following github-
500 repository: https://github.com/bjornarjensen/columbia-ga. Observation-based estimates for pCO$_2^{sea}$ and C$_{ant}$ are freely available at NOAA's
National Centers for Environmental Information via https://www.nodc.noaa.gov/ocads/oceans/SPCO2_1982_2015_ETH_SOM_FFN.html
and https://www.ncei.noaa.gov/data/oceans/ncei/ocads/data/0162565/mapped/, respectively. Our observational estimates of the contempo-
rary strength of northwards and southwards volume transports are based on data from the RAPID AMOC monitoring project, funded by the
Natural Environment Research Council and freely available from www.rapid.ac.uk/rapidmoc.

505 **Appendix A: Observational Estimates**

For observational estimates of the contemporary winter pCO$_2^{sea}$-anomaly (depicted in Fig. 1b-c and Fig. 8a-b), we utilised
a neural-network-based interpolated pCO$_2^{sea}$ product provided by Landschützer et al. (2017). Specifically, we calculated the
contemporary winter pCO$_2^{sea}$-anomaly as a decadal average based on the 'spco2_smoothed'-variable for the years 1990-1999.
We note that it would have been possible to focus on other time-frames. However, we decided to consider the same time-frames
510 as in Goris et al. (2018), so that an easy comparison of previous and new results is possible. As the utilised pCO$_2^{sea}$ database
does not include an error-estimate, we utilise the error-estimate of the supplementary information of Landschützer et al. (2018),
where the neural-network product is analysed for seasonal mean biases for 4 broad latitudinal bands. Results for summer and
winter biases of the data-product for the latitudinal bands of 10-40°N and 40-65°N show that the biases are randomly spread
around 0, but do show substantial variability. We apply the largest detected seasonal bias of these latitudinal bands of about
515 $\pm14\mu$atm as our uncertainty range of the observational estimate of the contemporary winter pCO$_2^{sea}$-anomaly.

For observational estimates of the contemporary fractional C$_{ant*}$-storage (depicted in Fig. 1d-e and Fig. 8d-e), the mapped
climatology of anthropogenic carbon (C$_{ant}$) from GLODAPv2.2016b has been used (Lauvset et al., 2016). We note that there
is a difference between this data-product and our modelled estimates as the data product describes C$_{ant}$ and the modelled esti-
mates C$_{ant*}$, i. e. a combination of the anthropogenic component of the carbon cycle combined with climate change–induced
520 differences. Yet, for the time span of the historical simulation, the climate-change induced differences are small and it is possi-
ble to use C$_{ant}$ as an approximation of C$_{ant*}$ (Frölicher et al., 2015). The observation-based data-product of the C$_{ant}$-storage
is normalized to the year 2002. We therefore compare it to the simulated fractional C$_{ant*}$-storage in the time-frame 1997-2007,
abbreviated as 1997s. For conversion of the data product from μmol/kg to PgC, we utilised a mean ocean standard density
of 1036kg/m^3 (Pawlowicz, 2013). Furthermore, we linearly interpolated the data-product onto the considered depth-levels.
525 Though the data-product includes estimates of a mapping error, a comprehensive error estimate containing observational,
methodological and mapping error is not available. In lack of such an estimate, we follow the approach of Goris et al. (2018)
and use an error estimate of $\pm10\%$ for the observational estimate of the fractional C$_{ant}$-storage below 1000m accumulated over
the whole North Atlantic (Fig. 1e). In order to get an error estimate for the fractional C$_{ant}$-storage within our optimal cuboids
and ellipsoids, we utilise the error-estimate of $\pm29\%$ for the C$_{ant}$-storage of the North Atlantic (Steinfeldt et al., 2009). The
530 simple assumption of an error of 29% for every grid point leads to the same factor in numerator and denominator and results in
an error estimate of zero for the fractional C$_{ant}$-storage. Only a spatially heterogeneously distributed error of the C$_{ant}$-storage
leads to a non-zero error estimate for the fractional C$_{ant}$-storage. As such an error estimate is missing, we simply assume

an error of $\pm$ 29% within our optimal areas but assume no error for other grid points of the North Atlantic, which are taken into account to build the fractional measure. When assuming an error of $\pm 29\%$ for the C_{ant}-values within our largest optimal cuboid, we obtain an error of +3.78% and -4.12% for the fractional C_{ant}-storage. In order to obtain an evenly distributed error around the mean value, we always chose the error-value larger in absolute values, yielding an error of e. g. $\pm 4.12\%$ for the largest cuboid. We follow the same procedure for the other optimal volumes.

For observational estimates of the contemporary strength of northward and southward volume transport (depicted in Fig. 8c,f), data from the RAPID-Meridional Overturning Circulation and Heatflux Array-Western Boundary Time Series array at 26°N have been employed (Frajka-Williams et al., 2021). RAPID-observations are only available from April 2004 onward, though our application of the genetic algorithm considers the years 1990-1999 (2D-case) and 1997-2007 (3D-case) for our regional optimisation. Due to lacking observations in the time-frames of interest, we build a decadal average of the observations of the AMOC streamfunction profile for the years 2005-2014. When needing to access accumulations of the streamfunction over differing depth ranges with boundaries at surface, 500m, 700m and 4700m, we are utilising the observed depths that are closest to these boundaries, i.e. surface, 496m, 694m and 4696m. We consider these depth-values to be close enough to the desired boundaries such that no interpolation is necessary. Annual error estimates between 0.9 and 1.3Sv are given for maximum northward transport estimates of the years 2004 to 2014 (https://rapid.ac.uk/rapidmoc/rapid_data/README_ERROR.pdf, accessed in November 2021). We employ the estimate of 1.3Sv as our observational error estimate. We note, however, that we are not utilising the maximum northward volume transport estimate directly but are accumulating differing depths of the streamfunction profile. This might lead to the error-estimate being imprecise.

Appendix B: Streamfunction values for our CMIP5 ensemble

Several of the here considered models did not provide the Atlantic Meridional Overturning Circulation to the CMIP5 database. Therefore, we utilised AMOC streamfunction values calculated with monthly mean meridional currents as described in Mecking et al. (2017).

Author contributions. NG, KJ and JT designed the application of the genetic algorithm. KJ implemented the genetic algorithm. NG prepared the ocean biogeochemical input data, extended the analysis to include the transport, illustrated the results and established and analysed the new emergent constraints. NG wrote the manuscript with assistance of KJ and JT.

Competing interests. The authors declare that they have no conflict of interest.

Acknowledgements. We would like to thank Jennifer Mecking for providing us with calculated AMOC streamfunction values for our model ensemble. This work was supported by the Norwegian Research Council through the project COLUMBIA (Grant 275268). We acknowledge

the World Climate Research Programme's Working Group on Coupled Modelling, which is responsible for CMIP, and we thank the climate modeling groups for producing and making available their model output. For CMIP, the U.S. Department of Energy's Program for Climate Model Diagnosis and Intercomparison provides coordinating support and led development of software infrastructure in partnership with the Global Organization for Earth System Science Portals. Data from the RAPID AMOC monitoring project is funded by the Natural
565 Environment Research Council and are freely available from www.rapid.ac.uk/rapidmoc.
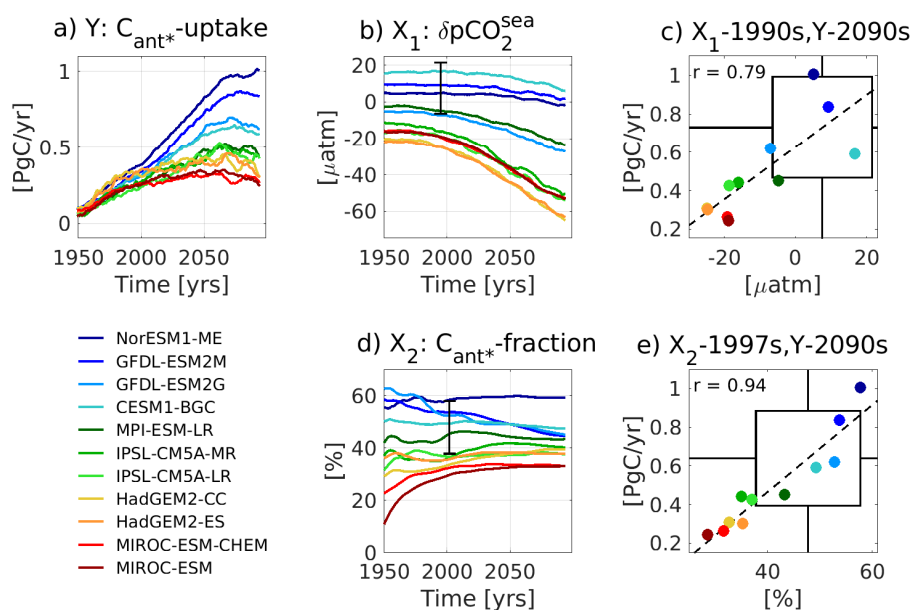
Figure 1. Illustration of two emergent constraints of the future North Atlantic C_{ant*}-uptake, both considering an ensemble of 11 CMIP5-models under a high CO_2 future. The color-coding of the ensemble is indicated in the legend. Panels (a,b,d) illustrate the temporal evolution in 10-year running averages for the (a) North Atlantic C_{ant*}-uptake (predictand Y), (b) mid-to-high latitude (35.5°N-75.5°N) winter pCO_2^{sea}-anomaly (predictor X_1) and its observational estimate (black error-bar in year 1995), (d) fraction of the North Atlantic C_{ant*} stored below 1000m depth (predictor X_2) and its observational estimate (black error-bar in year 2002). Panels (c,e) show scatter-plots, best fit linear regression, and cross-correlations between the predictors during the observational period (1990-1999 for X_1 and 1997-2007 for X_2) and future values of the predictand. Here, the mean observational constraint and its uncertainty are indicated by black (box-)lines parallel to the y-axis, while the observationally constrained mean value of the predictand and its uncertainty range are indicated by black (box-)lines parallel to the x-axis. See Appendix A for a detailed description of the considered observational estimates.
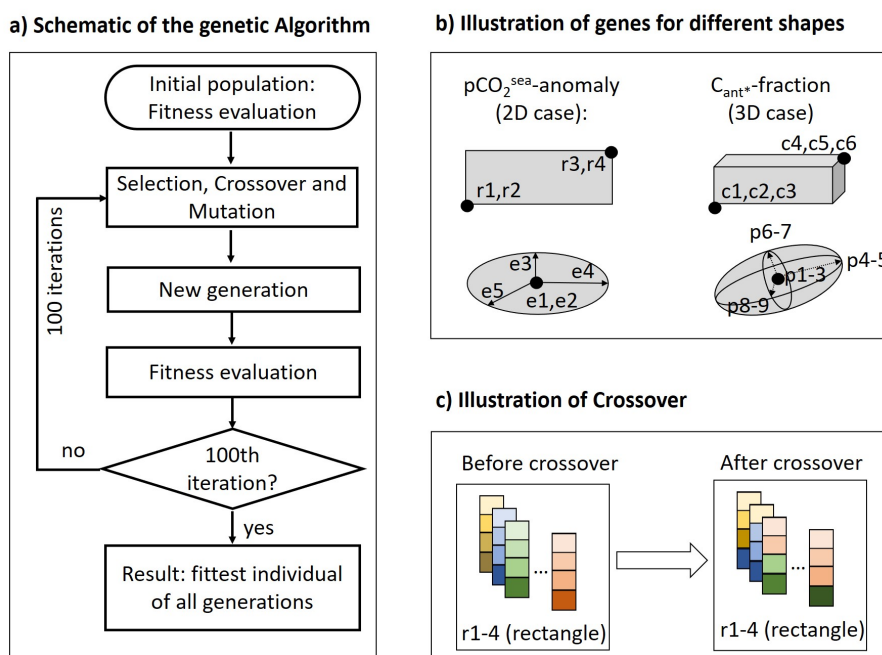
Figure 2. Schematic illustration for the experimental set-up of our application of the genetic algorithm. The panels illustrate a) one iteration of the algorithm, b) genes chosen to represent rectangles, ellipses, cuboids and ellipsoids as well as c) visualisation of a crossover for a population of rectangles.
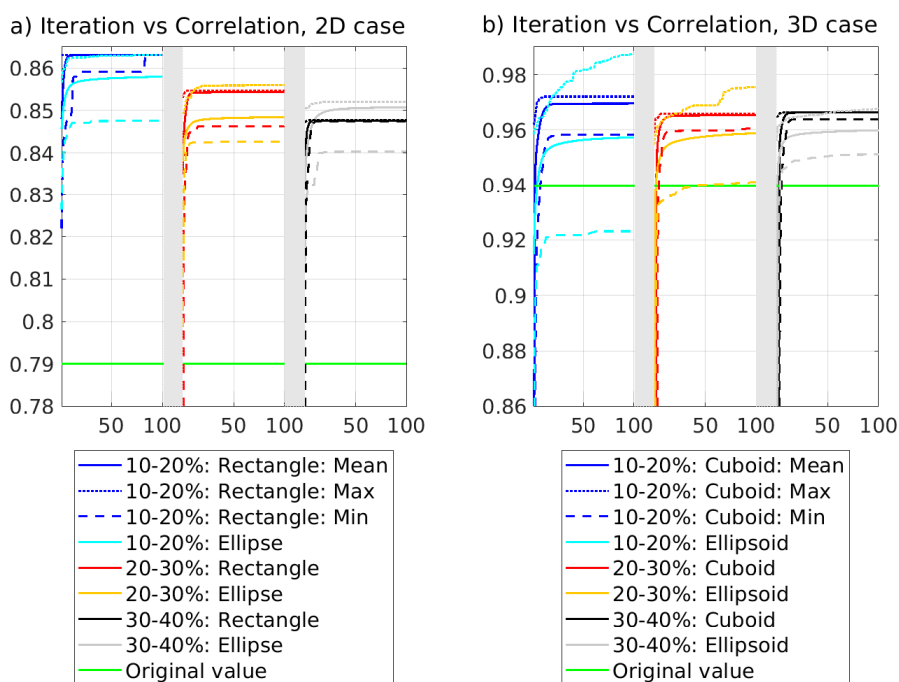
Figure 3. Iteration (population) versus cross-correlations for our application of the genetic algorithm. The correlation coefficients are calculated between contemporary values of the predictor within the regions identified by the genetic algorithm and future values of the predictand. The color-coding of the lines point towards the shapes and sizes that characterise these regions. Continuous/dashes lines identify the individual with the highest/lowest cross-correlation of each population, dotted lines identify the mean cross-correlation of each population. The green lines illustrates the cross-correlation without regional optimisation of the predictor.
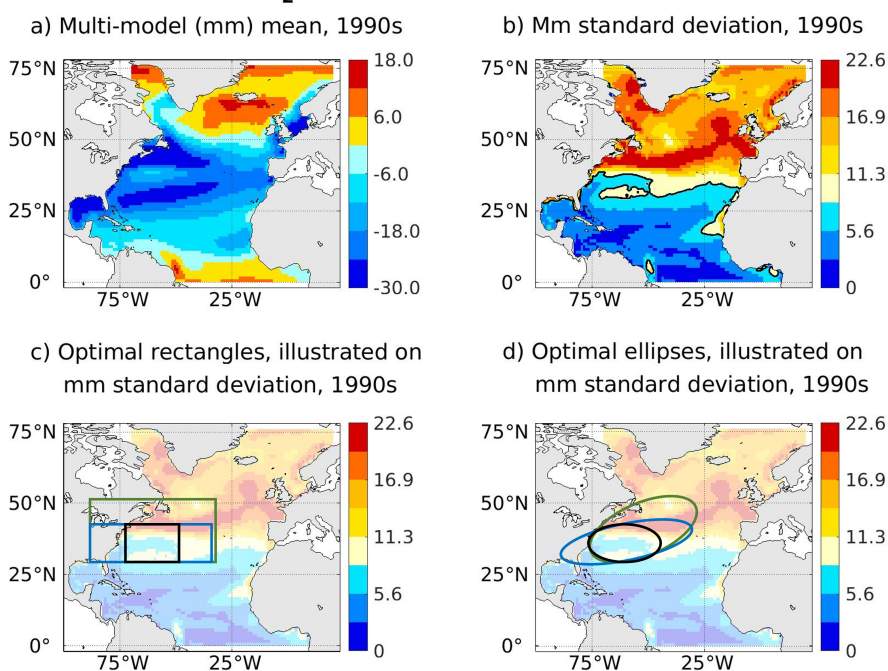
Figure 4. Contemporary winter pCO_2^{sea}-anomaly and associated optimal regions as identified by the genetic algorithm. For the contemporary winter pCO_2^{sea}-anomaly of our considered model-ensemble, panel (a) illustrates the multi-model mean, while panel (b) displays the multi-model standard deviation. Panels (c,d) display the optimal regions identified by the genetic algorithm on top of the multi-model standard deviation with non-eligible points colored in different shades of blue (separated with a black contour line in panel (b)). Optimal regions are visualised according to shapes, with panel (c) visualising rectangles and panel (d) visualising ellipses. The color-coding of the lines indicate different area-conditions that were imposed on the optimal areas (black lines: area-size of 10-20%, blue lines: area-size of 20-30% and green lines: area-size of 30-40% of the surface of the North Atlantic).
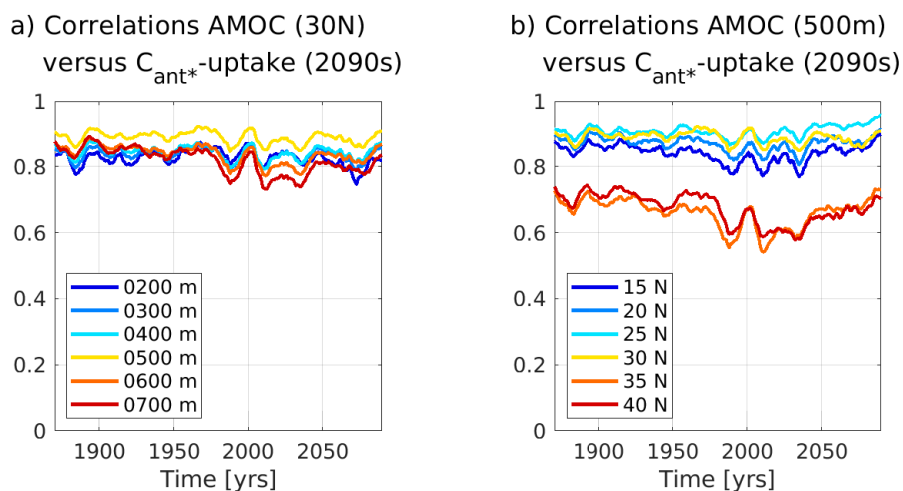
Figure 5. Time series of cross-correlations between 10-year running averages of the simulated upper branch of the Atlantic Meridional Overturning Circulation (AMOC) and the future North Atlantic C$_{ant*}$-uptake (2090s) for our model ensemble. The upper branch of the AMOC is expressed as accumulated northward volume transport between surface and a lower depth boundary at a certain latitude. Panel (a) shows results for 30°N and a varying lower depth boundary, while panel (b) shows results for a lower depth boundary of 500m and varying latitudes.
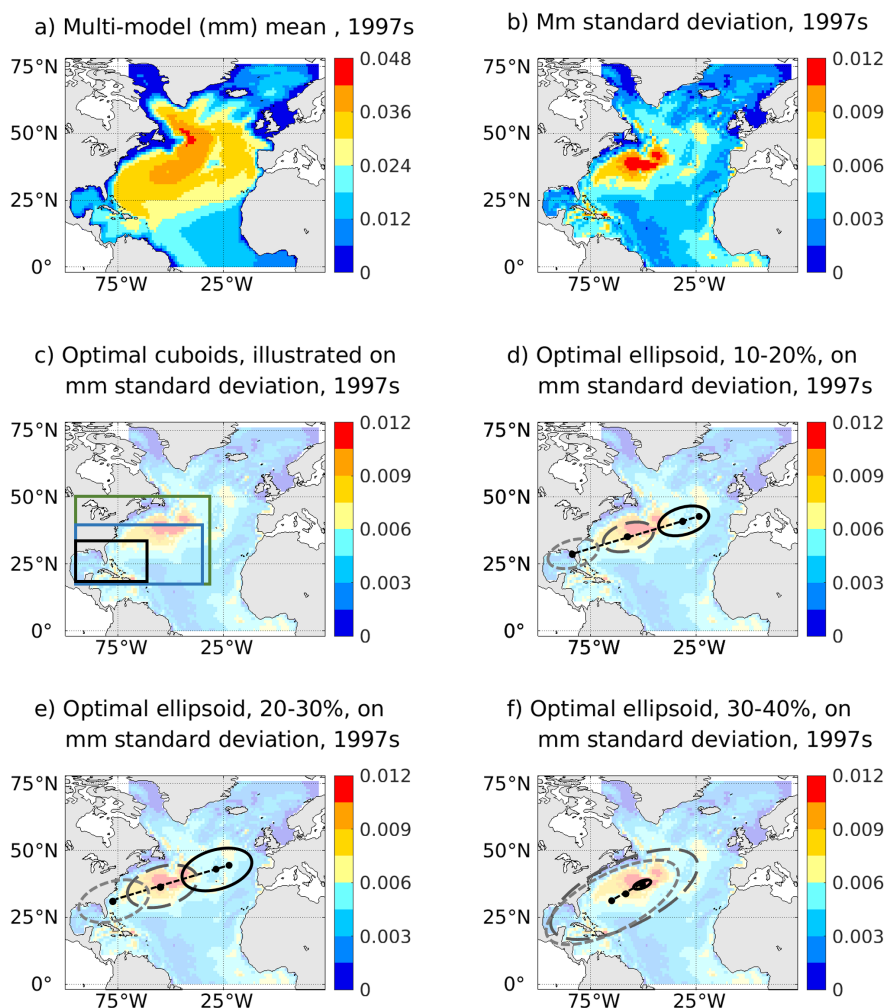
Figure 6. Contemporary fraction of the North Atlantic C_{ant*} and associated optimal regions as identified by the genetic algorithm. For the depth-integrated contemporary fraction of the North Atlantic C_{ant*} of our considered model-ensemble, panel (a) illustrates the multi-model mean, while panel (b) displays the multi-model standard deviation. Panels (c,d,e,f) display the optimal regions identified by the genetic algorithm on top of the multi-model standard deviation. Optimal regions are visualised according to shapes, with panel (c) visualising cuboids with volume-sizes of 10-20% (black lines), 20-30% (blue lines) and 30-40% (green lines) of the North Atlantic. Panels (d,e,f) visualise ellipsoids of different volumes via illustration of their mid-points (black dots) and outlines for the depth-planes 500-660m (black lines), 2500-2600m (dashed dark grey lines) and 4500-4600m (dashed light grey lines) and their depth-following principal axis (black line connecting the mid-points). In panels (d,e), the midpoint of the surface plane is additionally illustrated.
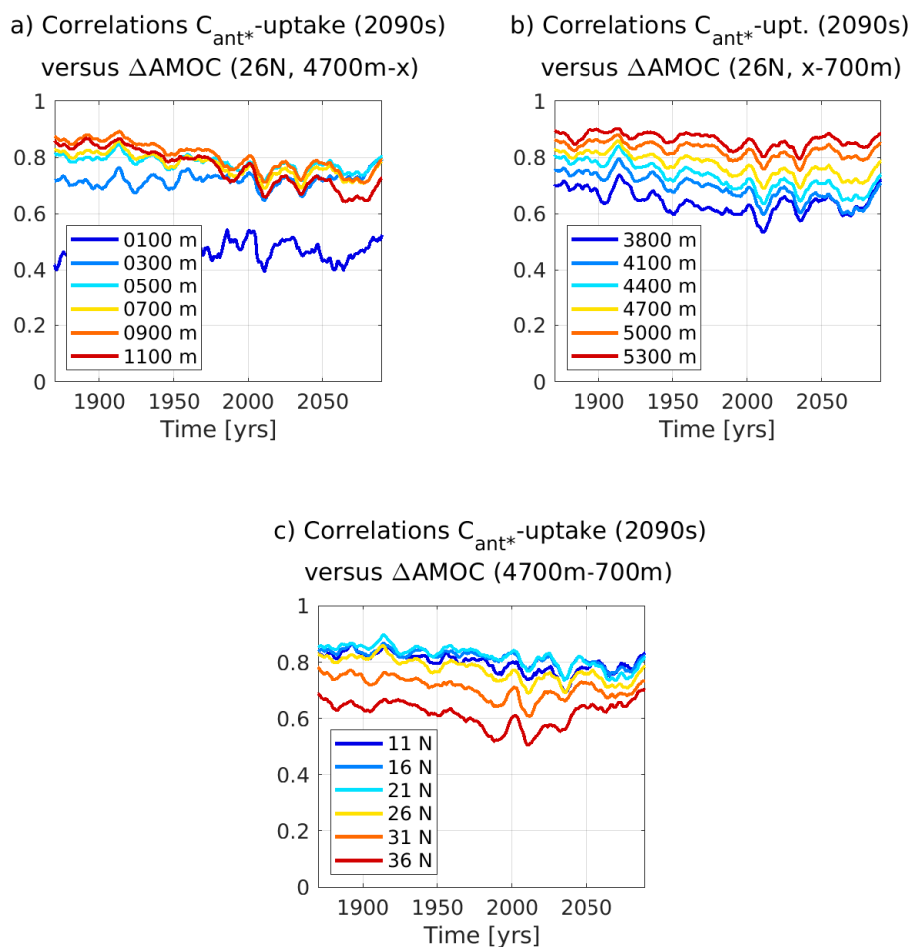
Figure 7. Time series of cross-correlations between 10-year running averages of the simulated lower branch of the Atlantic Meridional Overturning Circulation (AMOC) and the future North Atlantic C_{ant*}-uptake (2090s) for our model ensemble. The lower branch of the AMOC is expressed as accumulated southward volume transport between a higher depth boundary and a lower depth boundary at a certain latitude. Panel (a) shows results for 26°N, a lower depth boundary at 4700m and a varying higher depth boundary, while panel (b) shows results for 26°N, a higher depth boundary at 700m and a varying lower depth boundary and panel (c) for a higher depth boundary at 700m, a lower depth boundary at 4700m and varying latitudes.
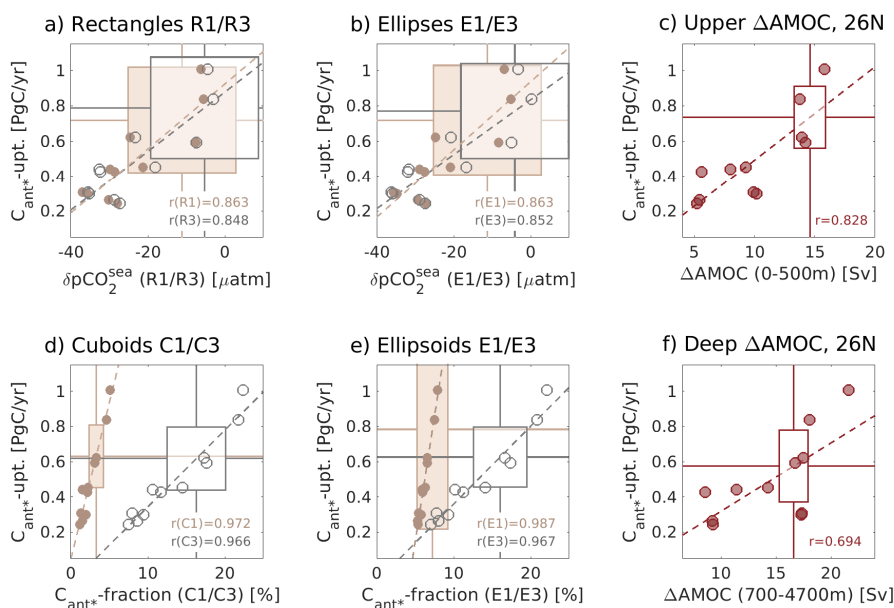
Figure 8. Illustration of emergent constraints between different regionally optimised predictors and the future North Atlantic C_{ant*}-uptake (predictand) for our model ensemble. All panels show scatter-plots, best fit linear regression, and cross-correlations between the predictors during the observational period and future values of the predictand. Here, the mean observational constraints and their uncertainties (see appendix A) are indicated by (box-)lines parallel to the y-axis, while the observationally constrained mean values of the predictand and their uncertainty ranges are indicated by (box-)lines parallel to the x-axis. Upper ocean predictors are visualised in the top panels including the winter pCO_2^{sea}-anomaly for different optimal areas (panels a-b, years 1990-1999) and the upper ocean northward volume transport (panel c, years 2005-2014). Bottom panels show water-column and deep ocean predictors, that is the fractional C_{ant*}-storage (panels d-e, years 1997-2007) and the deep ocean southward volume transport (panel f, years 2005-2014). In panels a-b and d-e, different sizes of the optimal areas are indicated with numbers (1: area-size of 10-20% and 3: area-size of 30-40% of the considered area) and associated coloring (coral lines for the smaller area and grey lines for the larger areas). Model-results are visualised via dots, following the same color code as the associated observational constraints.

Table 1. Constrained estimates of the future North Atlantic C_{ant*}-uptake based on regionally optimised predictors. Listed are the predictors, their realms (upper ocean: above 500m, deep ocean: below 500m depth) and considered time-frames as well as the associated constrained estimates of the future North Atlantic C_{ant*}-uptake. Different sizes of the optimal areas are indicated with numbers (1: area-size of 10-20%, 2: area-size of 20-30% and 3: area-size of 30-40% of the considered area).

predictor	realm	time-frame	constrained C_{ant*}-upt.
δpCO_2^{sea} (Ellipse E1)	upper ocean	1990-1999	0.72 ± 0.31 PgC/yr
δpCO_2^{sea} (Ellipse E2)	upper ocean	1990-1999	0.72 ± 0.28 PgC/yr
δpCO_2^{sea} (Ellipse E3)	upper ocean	1990-1999	0.77 ± 0.27 PgC/yr
δpCO_2^{sea} (Rectangle R1)	upper ocean	1990-1999	0.72 ± 0.30 PgC/yr
δpCO_2^{sea} (Rectangle R2)	upper ocean	1990-1999	0.73 ± 0.31 PgC/yr
δpCO_2^{sea} (Rectangle R3)	upper ocean	1990-1999	0.79 ± 0.29 PgC/yr
ΔAMOC, 26N (0-500m)	upper ocean	2005-2014	0.74 ± 0.18 PgC/yr
C_{ant*}-fraction (Ellipsoid E1)	water column	1997-2007	0.78 ± 0.57 PgC/yr
C_{ant*}-fraction (Ellipsoid E2)	water column	1997-2007	0.74 ± 0.39 PgC/yr
C_{ant*}-fraction (Ellipsoid E3)	deep ocean	1997-2007	0.63 ± 0.17 PgC/yr
C_{ant*}-fraction (Cuboid C1)	deep ocean	1997-2007	0.63 ± 0.18 PgC/yr
C_{ant*}-fraction (Cuboid C2)	deep ocean	1997-2007	0.62 ± 0.17 PgC/yr
C_{ant*}-fraction (Cuboid C3)	deep ocean	1997-2007	0.62 ± 0.18 PgC/yr
ΔAMOC, 26N (700-4700m)	deep ocean	2005-2014	0.57 ± 0.20 PgC/yr

References

Argo: Argo float data and metadata from Global Data Assembly Centre (Argo GDAC), https://doi.org/https://doi.org/10.17882/42182, 2000.

Balaji, V., Taylor, K. E., Juckes, M., Lawrence, B. N., Durack, P. J., Lautenschlager, M., Blanton, C., Cinquini, L., Denvil, S., Elkington, M., Guglielmo, F., Guilyardi, E., Hassell, D., Kharin, S., Kindermann, S., Nikonov, S., Radhakrishnan, A., Stockhause, M., Weigel, T., and Williams, D.: Requirements for a global data infrastructure in support of CMIP6, Geoscientific Model Development, 11, 3659–3680, https://doi.org/10.5194/gmd-11-3659-2018, 2018.

Bourgeois, T., Goris, N., Schwinger, J., and Tjiputra, J.: Stratification constrains future heat and carbon uptake in the Southern Ocean between 30°S and 55°S, Nature Communications, 13, https://doi.org/10.1038/s41467-022-27979-5, 2022.

Claustre, H., Bishop, J., Boss, E., Stewart, B., Berthon, J., Coatanoan, C., Johnson, K., Lotiker, A., Ulloa, O., Perry, M. J., D'Ortenzio, F., D'andon, O. H. F., and Uitz, J.: Bio-optical profiling floats as new observational tools for biogeochemical and ecosystem studies, in: Proceedings of the OceanObs'09: Sustained Ocean Observations and Information for Society Conference, Venice, 2010.

D'Ortenzio, F., Taillandier, V., Claustre, H., Prieur, L. M., Leymarie, E., Mignot, A., Poteau, A., Penkerc'h, C., and Schmechtig, C. M.: Biogeochemical Argo: The Test Case of the NAOS Mediterranean Array, Frontiers in Marine Science, 7, 120, https://doi.org/10.3389/fmars.2020.00120, https://www.frontiersin.org/article/10.3389/fmars.2020.00120, 2020.

Eiben, A. E. and Smith, J. E.: Introduction to Evolutionary Computing, Natural Computing Series, Springer, 2003.

Eyring, V., Bony, S., Meehl, G. A., Senior, C. A., Stevens, B., Stouffer, R. J., and Taylor, K. E.: Overview of the Coupled Model Intercomparison Project Phase 6 (CMIP6) experimental design and organization, Geoscientific Model Development, 9, 1937–1958, https://doi.org/10.5194/gmd-9-1937-2016, 2016a.

Eyring, V., Righi, M., Lauer, A., Evaldsson, M., Wenzel, S., Jones, C., Anav, A., Andrews, O., Cionni, I., Davin, E. L., Deser, C., Ehbrecht, C., Friedlingstein, P., Gleckler, P., Gottschaldt, K.-D., Hagemann, S., Juckes, M., Kindermann, S., Krasting, J., Kunert, D., Levine, R., Loew, A., Mäkelä, J., Martin, G., Mason, E., Phillips, A. S., Read, S., Rio, C., Roehrig, R., Senftleben, D., Sterl, A., van Ulft, L. H., Walton, J., Wang, S., and Williams, K. D.: ESMValTool (v1.0) – a community diagnostic and performance metrics tool for routine evaluation of Earth system models in CMIP, Geoscientific Model Development, 9, 1747–1802, https://doi.org/10.5194/gmd-9-1747-2016, 2016b.

Eyring, V., Cox, P. M., Flato, G. M., Gleckler, P. M., Abramowitz, G., Caldwell, P., Collins, W. D., Gier, B. K., Hall, A., Hoffman, F., Hurtt, G. C., Jahn, A., Jones, C. D., Klein, S. A., Krasting, J. P., Kwiatkowski, L., Lorenz, R., Maloney, E., Meehl, G. A., Pendergrass, A. G., Pincus, R., Ruane, A. C., Russell, J. L., Sanderson, B. M., Santer, B. D., Sherwood, S. C., Simpson, I. R., Stouffer, R. J., and Williamson, M. S.: Taking climate model evaluation to the next level, Nature Clim Change, 9, 102–110, https://doi.org/https://doi.org/10.1038/s41558-018-0355-y, 2019.

Frajka-Williams, E., Moat, B., Smeed, D., Rayner, D., Johns, W., Baringer, M., Volkov, D., and Collins, J.: Atlantic meridional overturning circulation observed by the RAPID-MOCHA-WBTS (RAPID-Meridional Overturning Circulation and Heatflux Array-Western Boundary Time Series) array at 26N from 2004 to 2020 (v2020.1), https://doi.org/10.5285/cc1e34b3-3385-662b-e053-6c86abc03444, 2021.

Frölicher, T. L., Sarmiento, J. L., Paynter, D. J., Dunne, J. P., Krasting, J. P., and Winton, M.: Dominance of the Southern Ocean in Anthropogenic Carbon and Heat Uptake in CMIP5 Models, J. Climate, 28, 862–886, https://doi.org/http://dx.doi.org/10.1175/JCLI-D-14-00117.1, 2015.

Gary, S. F., Lozier, M. S., Böning, C. W., and Biastoch, A.: Deciphering the pathways for the deep limb of the Meridional Overturning Circulation, Deep Sea Research Part II: Topical Studies in Oceanography, 58, 1781–1797, https://doi.org/https://doi.org/10.1016/j.dsr2.2010.10.059, 2011.

Goris, N., Tjiputra, J., Olsen, A., Schwinger, J., Lauvset, S., and Jeansson, E.: Constraining Projection-Based Estimates of the Future North Atlantic Carbon Uptake, Journal of Climate, 31, 3959–3978, https://doi.org/10.1175/JCLI-D-17-0564.1, 2018.

Hall, A., Cox, P., Huntingford, C., and Klein, S.: Progressing emergent constraints on future climate change, Nat. Clim. Change, 9, 269–278, https://doi.org/https://doi.org/10.1038/s41558-019-0436-6, 2019.

Holland, J. H.: Adaptation in natural and artificial systems: An introductory analysis with applications to biology, control, and artificial intelligence, University of Michigan Press, 1975.

IPCC: Climate Change 2013: The Physical Science Basis, in: Fifth Assessment Report of the Intergovernmental Panel on Climate Change, edited by Stocker, T., Qin, D., Plattner, G.-K., Tignor, M., Allen, S. K., Boschung, J., Nauels, A., Xia, Y., Bex, V., and Midgley, P. M., p. 1535, Cambridge University Press, Cambridge, United Kingdom and New York, USA, doi:10.1017/CBO9781107415324, 2013.

IPCC: Summary for Policymakers, in: Global Warming of 1.5°C. An IPCC Special Report on the impacts of global warming of 1.5°C above pre-industrial levels and related global greenhouse gas emission pathways, in the context of strengthening the global response to the threat of climate change, sustainable development, and efforts to eradicate poverty, edited by Masson-Delmotte, V., Zhai, P., Pörtner, H.-O., Roberts, D., Skea, J., Shukla, P., Pirani, A., Moufouma-Okia, W., Pean, C., Pidcock, R., Connors, S., Matthews, J., Chen, Y., Zhou, X., Gomis, M., Lonnoy, E., Maycock, T., Tignor, M., and Waterfield, T., World Meteorological Organization, Geneva, Switzerland, 2018.

Kessler, A. and Tjiputra, J.: The Southern Ocean as a constraint to reduce uncertainty in future ocean carbon sinks, Earth Syst. Dynam., 7, 295–312, https://doi.org/10.5194/esd-7-295-2016, 2016.

Kramer, O.: Genetic Algorithm Essentials, pp. 11–19, Springer International Publishing, https://doi.org/10.1007/978-3-319-52156-5_2, 2017.

Landschützer, P., Gruber, N., and Bakker, D.: An updated observation-based global monthly gridded sea surface pCO_2 and air-sea CO_2 flux product from 1982 through 2015 and its monthly climatology (NCEI Accession 0160558). Version 2.2., https://www.nodc.noaa.gov/ocads/oceans/SPCO2_1982_2015_ETH_SOM_FFN.html, 2017.

Landschützer, P., Gruber, N., Bakker, D. C. E., Stemmler, I., and Six, K. D.: Strengthening seasonal marine CO_2 variations due to increasing atmospheric CO_2, Nature Climate Change, 8, 146–150, https://doi.org/https://doi.org/10.1038/s41558-017-0057-x, 2018.

Landschützer, P., Laruelle, G. G., Roobaert, A., and Regnier, P.: A uniform pCO_2 climatology combining open and coastal oceans, Earth System Science Data, 12, 2537–2553, https://doi.org/10.5194/essd-12-2537-2020, https://essd.copernicus.org/articles/12/2537/2020/, 2020.

Lauvset, S. K., Key, R. M., Olsen, A., van Heuven, S., Velo, A., Lin, X., Schirnick, C., Kozyr, A., Tanhua, T., Hoppema, M., Jutterström, S., Steinfeldt, R., Jeansson, E., Ishii, M., Perez, F. F., Suzuki, T., and Watelet, S.: A new global interior ocean mapped climatology: the $1° \times 1°$ GLODAP version 2, Earth Syst. Sci. Data, 8, 325–340, https://doi.org/10.5194/essd-8-325-2016, 2016.

Mecking, J. V., Drijfhout, S. S., Jackson, L. C., and Andrews, M. B.: The effect of model bias on Atlantic freshwater transport and implications for AMOC bi-stability, Tellus A: Dynamic Meteorology and Oceanography, 69, https://doi.org/10.1080/16000870.2017.1299910, 2017.

Meehl, G. A., Boer, G. J., Covey, C., Latif, M., and Stouffer, R. J.: Intercomparison makes for a better climate model, Eos, 78, 445–451, 1997.

Meehl, G. A., Boer, G. J., Covey, C., Latif, M., and Stouffer, R. J.: The Coupled Model Intercomparison Project (CMIP), B. Am. Meteorol. Soc., 81, 313–318, 2000.

Meehl, G. A., Senior, C. A., Eyring, V., Flato, G., Lamarque, J.-F., Stouffer, R. J., Taylor, K. E., and Schlund, M.: Context for interpreting equilibrium climate sensitivity and transient climate response from the CMIP6 Earth system models, Science Advances, 6, https://doi.org/10.1126/sciadv.aba1981, 2020.

640   Mikaloff Fletcher, S. E., Gruber, N. P., and Jacobson, A.: Ocean Inversion Project how-to document, Report, Inst. for Geophys. and Planet. Phys., Univ. of Calif., Los Angeles, version 1.0, 2003.

Olsen, A., Brown, K. R., Chierici, M., Johannessen, T., and Neill, C.: Sea-surface CO_2 fugacity in the subpolar North Atlantic, Biogeosciences, 5, 535–547, https://doi.org/10.5194/bg-5-535-2008, https://bg.copernicus.org/articles/5/535/2008/, 2008.

Pawlowicz, R.: Key Physical Variables in the Ocean: Temperature, Salinity, and Density, Nature Education Knowledge, 4, 2013.

645   Petrie, R., Denvil, S., Ames, S., Levavasseur, G., Fiore, S., Allen, C., Antonio, F., Berger, K., Bretonnière, P.-A., Cinquini, L., Dart, E., Dwarakanath, P., Druken, K., Evans, B., Franchistéguy, L., Gardoll, S., Gerbier, E., Greenslade, M., Hassell, D., Iwi, A., Juckes, M., Kindermann, S., Lacinski, L., Mirto, M., Nasser, A. B., Nassisi, P., Nienhouse, E., Nikonov, S., Nuzzo, A., Richards, C., Ridzwan, S., Rixen, M., Serradell, K., Snow, K., Stephens, A., Stockhause, M., Vahlenkamp, H., and Wagner, R.: Coordinating an operational data distribution network for CMIP6 data, Geoscientific Model Development, 14, 629–644, https://doi.org/10.5194/gmd-14-629-2021, 2021.

650   Rhein, M., Kieke, D., Hüttl-Kabus, S., Roessler, A., Mertens, C., Meissner, R., Klein, B., Böning, C. W., and Yashayaev, I.: Deep water formation, the subpolar gyre, and the meridional overturning circulation in the subpolar North Atlantic, Deep Sea Research Part II: Topical Studies in Oceanography, 58, 1819–1832, https://doi.org/https://doi.org/10.1016/j.dsr2.2010.10.061, 2011.

Sastry, K., Goldberg, D., and Kendall, G.: Genetic Algorithms, in: Search Methodologies, edited by Burke, E. K. and Kendall, G., Springer, Boston, MA, https://doi.org/10.1007/0-387-28356-0_4, 2005.

655   Sivanandam, S. N. and Deepa, S. N.: Introduction to Genetic Algorithms, Springer Publishing Company, Incorporated, 1st edn., 2007.

Steinfeldt, R., Rhein, M., Bullister, J. L., and Tanhua, T.: Inventory changes in anthropogenic carbon from 1997–2003 in the Atlantic Ocean between 20°S and 65°N, Global Biogeochemical Cycles, 23, https://doi.org/10.1029/2008GB003311, http://dx.doi.org/10.1029/2008GB003311, 2009.

Tjiputra, J. F., Assmann, K., and Heinze, C.: Anthropogenic carbon dynamics in the changing ocean, Ocean Science, 6, 605–614,
660   https://doi.org/10.5194/os-6-605-2010, https://www.ocean-sci.net/6/605/2010/, 2010.

Tjiputra, J. F., Olsen, A., Assmann, K., Pfeil, B., and Heinze, C.: A model study of the seasonal and long-term North Atlantic surface pCO_2 variability, Biogeosciences, 9, 907–923, https://doi.org/10.5194/bg-9-907-2012, https://bg.copernicus.org/articles/9/907/2012/, 2012.

Wang, Z. A., Moustahfid, H., Mueller, A. V., Michel, A. P. M., Mowlem, M., Glazer, B. T., Mooney, T. A., Michaels, W., McQuillan, J. S., Robidart, J. C., Churchill, J., Sourisseau, M., Daniel, A., Schaap, A., Monk, S., Friedman, K., and Brehmer, P.: Advancing Observation of
665   Ocean Biogeochemistry, Biology, and Ecosystems With Cost-Effective in situ Sensing Technologies, Frontiers in Marine Science, 6, 519, https://doi.org/10.3389/fmars.2019.00519, 2019.

Weller, R. A., Baker, D. J., Glackin, M. M., Roberts, S. J., Schmitt, R. W., Twigg, E. S., and Vimont, D. J.: The Challenge of Sustaining Ocean Observations, Frontiers in Marine Science, 6, 105, https://doi.org/10.3389/fmars.2019.00105, https://www.frontiersin.org/article/10.3389/fmars.2019.00105, 2019.

670   Williams, R. G., McDonagh, E., Roussenov, V. M., Torres-Valdes, S., King, B., Sanders, R., and Hansell, D. A.: Nutrient streams in the North Atlantic: Advective pathways of inorganic and dissolved organic nutrients, Global Biogeochemical Cycles, 25, https://doi.org/https://doi.org/10.1029/2010GB003853, 2011.

Williamson, M. S., Thackeray, C. W., Cox, P. M., Hall, A., Huntingford, C., and Nijsse, F. J. M. M.: Emergent constraints on climate sensitivities, Reviews Of Modern Physics, 93, https://doi.org/10.1103/RevModPhys.93.025004, 2021.